Received: 1 April 2023 | Revised: 16 June 2023 | Accepted: 4 July 2023

DOI: 10.1002/mrm.29805

RESEARCH ARTICLE

Magnetic Resonance in Medicine

Diffusion-weighted SPECIAL improves the detection of J-coupled metabolites at ultrahigh magnetic field

Jessie Mosso[1,2,3] | **Dunja Simicic**[2,3] | **Bernard Lanz**[2,3] | **Rolf Gruetter**[1] | **Cristina Cudalbu**[2,3]

[1]LIFMET, EPFL, Lausanne, Switzerland

[2]CIBM Center for Biomedical Imaging, Lausanne, Switzerland

[3]Animal Imaging and Technology, EPFL, Lausanne, Switzerland

Correspondence
Jessie Mosso, LIFMET, EPFL, Lausanne, Switzerland.
Email: jessie.mosso@epfl.ch

Funding information
CIBM Center for Biomedical Imaging; Ecole polytechnique fédérale de Lausanne (EPFL); H2020 Marie Skłodowska-Curie Actions, Grant/Award Number: 813120; Schweizerischer Nationalfonds zur Förderung der Wissenschaftlichen Forschung, Grant/Award Numbers: 310030_173222, 310030_201218

Abstract

Purpose: To improve the detection and subsequent estimation of the diffusion properties of strongly J-coupled metabolites in diffusion-weighted MRS (DWS).

Methods: A new sequence for single-voxel diffusion-weighted ^{1}H MR spectroscopy, named *DW-SPECIAL*, is proposed. It combines the semi-adiabatic SPECIAL sequence with a stimulated echo diffusion block. Acquisitions with DW-SPECIAL and STE-LASER, the current gold standard for rodent DWS experiments at high fields, were performed at 14.1T on phantoms and in vivo on the rat brain. The apparent diffusion coefficient and intra-stick diffusivity (Callaghan's model, randomly-oriented sticks) were fitted and compared between the sequences for glutamate, glutamine, myo-inositol, taurine, total NAA, total Cho, total Cr, and the macromolecules.

Results: The shorter TE achieved with DW-SPECIAL (18 ms against 33 ms with STE-LASER) substantially limited the metabolites' signal loss caused by J-evolution. In addition, DW-SPECIAL preserved the main advantages of STE-LASER: absence of cross-terms, diffusion time during a stimulated echo, and limited sensitivity to B_1 inhomogeneities. In vivo, compared to STE-LASER, DW-SPECIAL yielded the same spectral quality and reduced the Cramer Rao Lower Bounds for J-coupled metabolites, irrespective of the *b*-value. DW-SPECIAL also reduced the SD of the metabolites' diffusion estimates based on individual animal fitting without loss of accuracy compared to the fit on the averaged decay.

Conclusion: We conclude that due to its reduced TE, DW-SPECIAL can serve as an alternative to STE-LASER when strongly J-coupled metabolites like glutamine are investigated, thereby extending the range of accessible metabolites in the context of DWS acquisitions.

KEYWORDS

diffusion-weighted MRS, glutamine, J-coupled metabolites, rat brain, SPECIAL sequence

1 | INTRODUCTION

In vivo diffusion-weighted MRS (DWS) and DWI have emerged as powerful techniques to probe tissue morphology at the micrometer scale via the noninvasive assessment of a variety of diffusion metrics.[1–4] By inserting diffusion-sensitizing gradients into traditional single-voxel ^{1}H MR spectroscopy sequences, the diffusion properties of metabolites measured by MRS can be retrieved. Investigating the deviation of these diffusion properties from those expected for free diffusion allows one to infer the environment that a given metabolite is experiencing.

Contrary to water measured with DWI, brain metabolites detectable by MRS are mostly intracellular, and some of them are believed to be cell-specific: myo-inositol (mIns) and glutamine (Gln) are predominantly located in the astrocytes, and NAA and glutamate (Glu) in the neurons.[5–7] Given this prior knowledge, DWS has the potential to provide unique cell-specific microstructural information, synergetic to the nonspecific yet more sensitive information obtained from DWI probing water molecules located in all cell types and exchanging between compartments.

Since the pioneering work in animals and humans,[8,9] DWS has explored and revealed microscopic signatures of brain cells.[10–13] Neurons,[14] astrocytes,[15] and microglia[16] and their alterations in disease populations have been investigated with DWS, also in cases in which DWI failed to probe any change due to its non-cell–specific nature.[15]

However, unlike DWI, DWS suffers from low sensitivity due the low concentration of metabolites compared to water. It is thus important to improve DWS experiments at the acquisition and processing levels, as highlighted in a recent consensus effort.[17]

Traditionally, DWS has been performed using diffusion-weighted (DW-) PRESS or STEAM sequences. Both sequences have their respective advantages and disadvantages: DW-PRESS benefits from full-signal intensity but is impacted by signal losses from the transverse magnetization during the diffusion time due to T_2 relaxation and J-evolution, and by the limitations of the nonadiabatic 180° pulses at high fields (chemical shift displacement [CSD] artifacts, sensitivity to B_1 inhomogeneities with surface coils, high power deposition). DW-STEAM benefits from the slow T_1 relaxation of the longitudinal magnetization originating the signal during the diffusion time and from better RF pulse selection properties by using only 90° pulses but has the drawback of the resulting halved signal intensity. Additionally, both DW-STEAM and DW-PRESS are affected by cross-terms, namely contributions to the b-value proportional to $\boldsymbol{g}_{\text{diff}}\cdot\boldsymbol{g}_{\text{other}}$ (where $\boldsymbol{g}_{\text{other}}$ stands for imaging/spoiler/crusher gradients), which need to be accounted for to accurately estimate the diffusion properties.

More recently, the DW-semi-LASER[18] (localization by adiabatic selective refocusing) and the stimulated echo (STE)-LASER[19] sequences have been introduced, both being based on the LASER[20,21] localization, whose adiabatic volume selection is generally recommended at high magnetic fields despite its high specific absorption rate (SAR).[22,23] STE-LASER became the gold-standard in rodent DWS studies: its block-design separates the STE diffusion module from the LASER localization and thus prevents the appearance of cross-terms, while preserving the other advantages of DW-STEAM.

However, the use of STE-LASER leads to longer TEs, thus hindering the detection limits of J-coupled metabolites. Currently, mostly singlets (NAA, total Cho [tCho], total Cr [tCr]) and few J-coupled metabolites (taurine [Tau], mIns) are reported in DWS studies. Gln, for example, is seldom investigated, owing to challenges in its quantification, even more so when the MRS signal is strongly weighted by diffusion: its overlap with Glu at fields < 9.4 T, a low concentration, and strong J-coupling. Yet, Gln is a desired target for DWS studies because it plays an important role in various pathologies and is an astrocyte-specific marker due to the exclusive location of glutamine synthetase in the astrocytes.[24] A striking example is hepatic encephalopathy, in which brain Gln is increased by more than 100% as a result of excessive ammonia reaching the brain.[25–28] In that context, DWS probed an increase in metabolite diffusivities, including in Gln, in the cerebellum of a rat model of the disease, consistent with the loss of neuronal and astrocytic internal structure observed by histology.[29,30] Yet, a reliable estimation of Gln diffusion properties in the control group, in which its concentration is not as high as in hepatic encephalopathy, still remains challenging.

The SPECIAL sequence[31] (spin echo, full intensity acquired localized spectroscopy) and its semi-adiabatic counterpart[32] have been introduced in animal and human ^{1}H MR spectroscopy studies to reach shorter TEs, and thus reduce signal loss by J-evolution and T_2 relaxation, and are among the sequences recommended by the MRS consensus papers recently published.[22,23] As compared to LASER, SPECIAL reintroduces partial sensitivity to B_1 inhomogeneities along the direction of the nonadiabatic slice-selective RF pulse, requires outer volume suppression (OVS), and can be sensitive to motion due to its 1D ISIS scheme (image-selected in vivo spectroscopy). However, the possibility to reach very short TEs while reducing the SAR promoted SPECIAL as an attractive alternative to LASER in single-voxel MRS, providing the most accurate quantitative information from a ^{1}H MR spectrum by

minimizing the J-evolution in coupled spin systems and reducing T_2 losses.[22,23]

Following this trend, we propose a new diffusion-weighted MRS sequence, the DW-SPECIAL sequence, based on the semi-adiabatic SPECIAL sequence combined with a STE diffusion block, with the aim of preserving the advantages of the gold-standard STE-LASER sequence in rodent DWS studies while reaching a shorter TE.

2 | METHODS

2.1 | Sequence design

The DW-SPECIAL combines a STE diffusion block with a semi-adiabatic SPECIAL[31,32] localization (sequence diagram in Figure 1). The first slice-selective 90° pulse is an asymmetric P10 pulse[33] (0.5 ms, 13.5 kHz bandwidth, 3.3 kHz $\gamma B_{1,max}$, numerically optimized, 5 lobes, 18% refocusing factor), with the gradient refocusing lobe applied before the first diffusion gradient to avoid cross-terms between these two gradients in the *b*-value (Figure S9) (Appendix). Two additional non-slice–selective 90° hard pulses (0.1 ms, 12.8 kHz bandwidth) are used to form the STE block. The adiabatic 180° pulses are hyperbolic-secant (HS) HS1-R20 pulses[21] (2 ms, 10 kHz bandwidth, 4.8 kHz $\gamma B_{1,max}$ for adiabatic inversion and rephasing). The slice-selective adiabatic inversion is inserted in the mixing time of the STE block and is applied in the direction with strongest B_1 inhomogeneity (here, the *y*-direction, perpendicular to the transmit/receive quadrature surface coil). It is alternatively switched on and off to perform the 1D ISIS scheme (a two-step phase cycling is required to obtain a spectrum). An additional water suppression Hermite pulse (15.4 ms, 350 Hz bandwidth, 89 Hz $\gamma B_{1,max}$) is inserted in the mixing time to saturate the water signal relaxing during the diffusion time. Bipolar diffusion gradients that minimize the effects of eddy currents are used around the two non-slice–selective 90° pulses. Spoiler and crusher gradient amplitudes were adjusted empirically to minimize spurious echoes and outer voxel contributions while limiting the additional unwanted diffusion-weighting created by crushers around the 180° pulses. The following phase cycling was used: $ph_{bp} = 0$, $ph_{HS,on/off} = \{0000000022222222\}^1$, $ph_{P10} = \{0000222200002222\}^1$, $ph_{HS} = \{0011223300112233\}^1$, $ph_{receive} = \{0202202002022020\}^3$ (Bruker's [Bruker BioSpin MRI GmbH, Ettlingen, Germany] nomenclature: phases in units of 90° in brace brackets, phase increment for the second cycle given by the exponent *n* (+ $n \times 90°$). The corresponding author (J.M.) is willing to share the sequence ready to use on Paravision 360 v1.1 and Paravision 360 v3.3 and to help adapt it to other versions of Bruker's software and to other field strengths and gradient systems.

2.2 | In vivo acquisitions

All experiments were approved by The Committee on Animal Experimentation for the Canton de Vaud, Switzerland (VD3022.1).

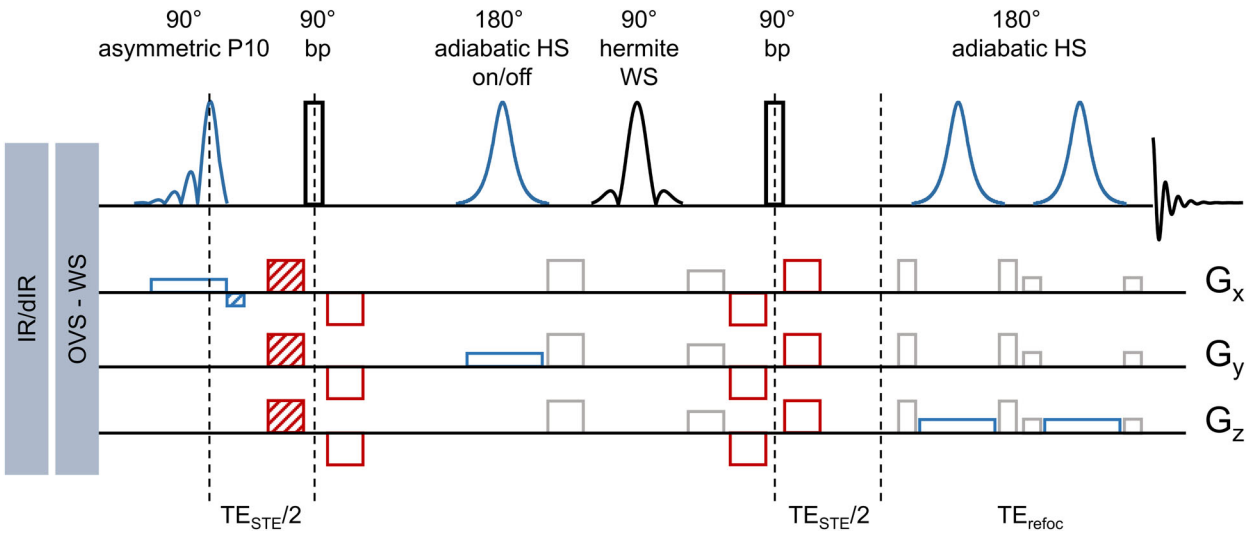

FIGURE 1 DW-SPECIAL sequence. (Row 1) RF pulses; those from the semi-adiabatic SPECIAL sequence are highlighted in blue. (Rows 2–4) Gradients—blue: slice-selection gradients, red: bipolar diffusion gradients, gray: spoiler/crusher gradients (arbitrary values displayed). WS, OVS, and (d-)IR modules are inserted before the first excitation pulse. The slice-refocusing gradient of the first slice-selective 90° pulse (blue) and the first diffusion gradients (red) are striped to indicate that they should not be applied simultaneously to avoid cross-terms in the *b*-value. The details of the RF pulses are provided in the Sequence design section (see 2.1) of the Methods section. DW, diffusion-weighted; (d-)IR, (double-) inversion recovery; OVS, outer volume suppression; SPECIAL, spin echo full intensity acquired localized spectroscopy; WS, water suppression.

Three adult male Wistar rats were scanned twice with a 2-week interval to acquire five diffusion sets (rat 1, rat 2, and rat 3 at week 0; rat 1 and rat 2 at week 2) and one macromolecules profile (rat 3 at week 2) with DW-SPECIAL and STE-LASER. During the DWS experiments, isoflurane anesthesia (~1.5%, in a 50%/50% air/O_2 mix, 0.9 L/min) was used, the respiration rate and the body temperature were monitored (SA Instruments, New York, NY), the latter being maintained at 37.7°C by circulating warm water.

Diffusion-weighted MRS experiments were performed on a 14.1T Bruker scanner (Avance Neo, Paravision 360 v1.1), with maximum gradient amplitude of 1 T/m (rise time: 270 µs), and a homemade transmit/receive quadrature surface RF coil (two loops of 20 mm diameter).

Anatomical MR images were acquired first to position the MRS voxel and define the shimming region using a localizer multi-slice gradient echo sequence (FOV: $25 \times 25\ mm^2$, $98 \times 98\ \mu m^2$ in-plane resolution, 15 slices/direction, slice thickness: 0.8 mm, slice gap: 1 mm, TE/TR: 2.92/18 ms, 1 average) and a T_2-TurboRARE sequence (FOV: $20 \times 20\ mm^2$, $78 \times 78\ \mu m^2$ in-plane resolution, 15 axial slices, slice thickness: 1 mm, slice gap: 0.2 mm, RARE factor 6, TE/TR: 27/3000 ms, 2 averages).

The position of the MRS voxel ($7 \times 5 \times 5\ mm^3$) is displayed in Figure 2. First- and second-order shimming were performed with the Bruker MAPSHIM method (shim values based on a measured map of the B_0 field in the object) followed by local iterative first-order shimming in the MRS voxel, leading to a water linewidth of 17–19 Hz. For the DW-SPECIAL acquisition, the shortest achievable TE was used (TE = 18.4 ms with $TE_{STE} = 8.9$ ms, $TE_{refoc} = 9.5$ ms, as labeled in Figure 1), and a mixing time of 40 ms, yielding a diffusion time (Δ) of 42.6 ms (characteristic 1D diffusion

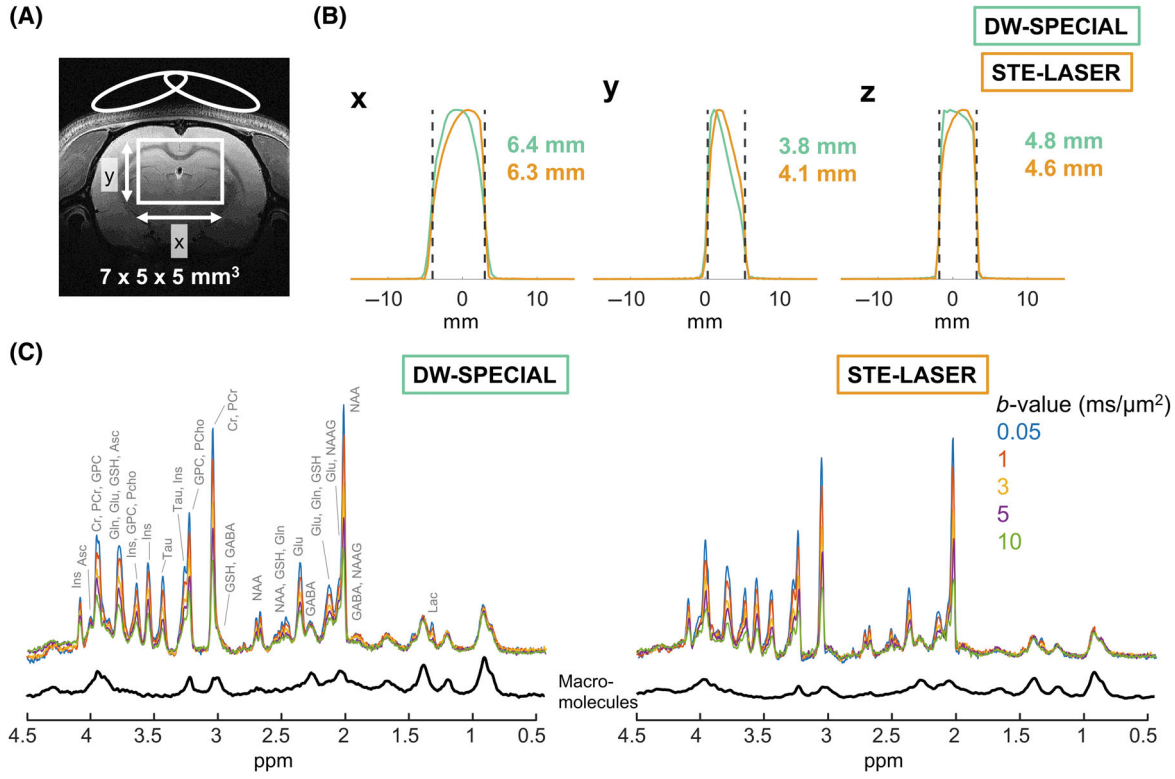

FIGURE 2 (A) Representative voxel location in one animal with *x*, *y* directions labeled: *y*, perpendicular to the plane of the surface coil, is the most inhomogeneous direction in B_1 amplitude. (B) 1D projections of voxel profiles on *x*, *y*, *z* normalized to 1 (obtained by switching on the corresponding gradient during the acquisition of the water signal) for DW-SPECIAL (green) and STE-LASER (orange), measured in the multi-metabolite phantom with a nominal voxel size of $7 \times 5 \times 5\ mm^3$. The VOI dimensions were approximated by numerical step-wise integration of the normalized voxel profiles y_i over the distance step $\left(\sum y_i \times \delta_{mm} \text{ where } \delta_{mm} = \frac{FOV[mm]}{\#points}\right)$. The dashed black lines represent the nominal voxel position in each direction (nominal position ± nominal size/2). (C) Representative in vivo ^1H MR spectra of DW-SPECIAL and STE-LASER pulse sequences for five *b*-values are displayed. Pre-processing with eddy currents correction, phase/frequency drift correction, outlier removal, and a 2 Hz line broadening were applied. Macromolecules are also displayed (black). Spectra amplitudes are normalized by the receiver gain, voxel size, and number of shots (same with both sequences): the remaining difference between DW-SPECIAL and STE-LASER diffusion sets amplitudes results from the additional loss by T_2 relaxation and J-evolution in STE-LASER. Voxel profiles were very similar on *x* and *z*. On *y*, the more B_1-inhomogeneous direction, STE-LASER selected more signal distant from the coil (toward *y* positive). The diffusion sets and macromolecules with both sequences were of good quality. LASER, localization by adiabatic selective refocusing; VOI, volume of interest.

length of ≈3.5 μm). The minimum TE_{refoc} was in fact 8.4 ms but was slightly increased to 9.5 ms to prevent baseline distortions. The STE-LASER sequence[19] was used for comparison with its respective minimum achievable TE of 33.7 ms (TE_{STE} = 8.7 ms, TE_{refoc} = 25 ms) and a mixing time of 40 ms, yielding a diffusion time (Δ) of 43.4 ms.

For both sequences, the diffusion gradients duration (δ) was set to 3 ms. The following *b*-values in the direction (1) were used: 0.05, 1, 3, 5, 10, and 30 ms/μm² for STE-LASER; and 0.05, 0.94, 2.8, 4.7, 9.4, and 28.2 ms/μm² for DW-SPECIAL. The last *b*-value was acquired in one animal only as proof of feasibility. The mismatched *b*-values between DW-SPECIAL and STE-LASER were not intended: for clarity, only the round values from STE-LASER will be referred to in the following text, but the true *b*-values were used for fitting and display. The following other acquisition parameters were used identically for the two sequences: TR = 3000 ms, 4096 complex points, 7142 Hz of spectral width, carrier frequency for excitation of water-suppressed signals at 3 ppm.

The number of metabolites shots (NS) for DWS acquisitions was NS = 160 for *b*-values up to 5 ms/μm² and was increased to 320 for *b* = 10 ms/μm² and 30 ms/μm² to compensate for the SNR drop caused by the high *b*-values and potentially additional motion-corrupted shots removed during postprocessing. The VAPOR (variable pulse power and optimized relaxation delays water suppression) water suppression module[33] (pulse bandwidth: 350 Hz, last delay: 22.8 ms, flip angles 1 and 2: 84°/150°) was optimized and interleaved with OVS pulses in both DW-SPECIAL and STE-LASER (6 OVS slabs, slab thickness: 12 mm, gap to voxel: 0.3 mm, sech pulse [1 ms], OVS crusher gradients [x/y/z: 150/250/350 mT/m, 3 ms]). A reference non-water–suppressed spectrum was acquired for eddy currents correction, and between-scan B_0 drift compensation was performed with a navigator scan. Each *b*-value was acquired in full as single shots and in a random order between sequences and *b*-values. The total duration of the scan per animal was approximately 2 h 30 min (MRI and adjustments: 30 min, diffusion set per sequence: 60 min).

The term *shot* will be used throughout the manuscript to refer to each MRS complex FID acquired and stored individually (e.g., two shots are needed to complete the 1D ISIS scheme).[34]

2.3 | Phantom acquisitions

Phantom experiments were performed to validate the J-evolution observed in the simulated basis set. Three phantoms were prepared ([a] 8 mM Gln, [b] 8 mM γ-aminobutyric acid [GABA], [c] 8 mM mIns + 8 mM Cr, with 0.5 mM DSS in PBS) and scanned with the same sequence parameters at *b* = 0.05 ms/μm². A diffusion acquisition on a fourth phantom containing all the metabolites observed in vivo (see the Processing section of the Methods part) with realistic concentrations was also performed. The diffusion attenuation of mIns, Tau, Glu, and tCr signals in solution were measured with DW-SPECIAL and STE-LASER to validate experimentally the absence of cross-terms in DW-SPECIAL. The same sequence parameters as for the in vivo acquisitions were used, except for the *b*-values, which were the following: 0.05, 0.1, 0.3, 0.5, 1, 1.5, 2, 2.5, 3, 3.5, and 4 ms/μm².

2.4 | Processing

The same processing was applied for the two sequences. Individual shots were corrected for EC with the water signal. Phase and frequency drifts were performed simultaneously with spectral registration in FID-A[35] (time domain, spectral region restricted to the NAA peak at 2.01 ppm, aligned to the median of the shots, 12 Hz line broadening for processing only), followed by motion-corrupted shots removal (z_i: square difference between the real part of spectrum *i* and the real part of the median spectrum, averaged over spectral points. Rejection criterion: $\frac{z_i - \bar{z}}{SD(z)} > 1.5$, in which $\bar{z}$ and $SD(z)$ are the mean and SD of z_i across shots). For DW-SPECIAL, the above-mentioned processing was applied separately on odd and even shots—and if one shot was corrupted and removed, its corresponding on/off shot from the 1D ISIS scheme was also removed (Figure S1). A metabolite basis-set was simulated for each sequence with NMRScope-B[36] (jMRUI[37,38]: http://www.jmrui.eu), using the exact RF pulse shapes and delays. It included: alanine (Ala), ascorbate (Asc), aspartate (Asp), β-hydroxybutyrate (bHB), glycerophosphocholine (GPC), phosphocholine (PCho), Cr, PCr, GABA, glucose (Glc), Gln, Glu, glutathione (GSH), mIns, lactate (Lac), NAA, N-acetylaspartylglutamate (NAAG), phosphoethanolamine (PE), scyllo-inositol (Scyllo), and Tau using previously published J-coupling constants and chemical shifts.[39–41] Metabolite signal amplitudes were quantified with LCModel, and the diffusion coefficients were fitted only for the metabolites with Cramer Rao Lower Bounds (CRLB) below 5% at *b* = 0.05 ms/μm² (Glu, mIns, Tau, total NAA (tNAA, NAA + NAAG), tCr (Cr + PCr), tCho (GPC + PCho), and the mobile macromolecules [MM]) and Gln (CRLB = 6.4 ± 0.5%).

The macromolecules displayed in Figure 2 were acquired in the same voxel in one animal using double inversion-recovery and diffusion-weighting[42] (TE = 18.5 ms, TR = 4000 ms, TI = 2200/850 ms for DW-SPECIAL and TI = 2200/800 ms for STE-LASER, 7 blocks of 64 shots, *b* = 10 ms/μm²); and metabolites residuals were removed using AMARES[43] from jMRUI, as described previously.[44] The metabolites residual patterns

were further confirmed with the acquisition of MM spectra at multiple inversion times and with/without diffusion gradients (Figure S2).

A detailed table of the acquisition and processing parameters following the International Society for Magnetic Resonance in Medecine experts' consensus recommendations on minimum reporting standards in in vivo MRS[45] is presented in Table S5.

2.5 | Fitting

A Gaussian diffusion model $\left(\frac{S}{S_0} = e^{-b \cdot ADC}\right)$ up to $b = 3\,\text{ms}/\mu\text{m}^2$ and the randomly oriented sticks model[46] $\left(\frac{S}{S_0} = \sqrt{\frac{\pi}{4bD_{\text{intra}}}}\,\text{erf}\left(\sqrt{bD_{\text{intra}}}\right)\right)$ up to $b = 10\,\text{ms}/\mu\text{m}^2$ were fitted to each metabolite signal diffusion decay as a function of b-value. The fits were performed individually for each animal and on the averaged metabolite signal diffusion decay normalized to its value at $b = 0.05\,\text{ms}/\mu\text{m}^2$, the latter being referred to as *mean fit*. A nonlinear least squares algorithm was used (MatLab R2023a *fit* function, trust-region method) (MathWorks, Natick, MA), weighted with the inverse of absolute CRLB for the individual fit case, and with the inverse of the SD of each normalized signal amplitude across animals for the *mean fit* case.

2.6 | Statistics

The ADC and the intra-stick diffusion coefficient (D_{intra}) are reported as mean and SD across animals, and with their corresponding value fitted from the mean decay. We approximated that the two rats scanned twice with a 2-week interval and used for the diffusion sets could be considered as independent samples for statistics.

A two-way repeated measures analysis of variance (ANOVA) was performed on the ADC and D_{intra} values fitted on the metabolite signal diffusion decays of individual animals, comparing the sequence effect for all metabolites, with animal-matched values and Bonferroni multiple comparisons post hoc test. For a given metabolite, an F-test was performed to compare the SD across animals of the normalized signal decays at $b = 3\,\text{ms}/\mu\text{m}^2$ and $b = 10\,\text{ms}/\mu\text{m}^2$ and the SD across animals of the estimated ADC and D_{intra}, between the two sequences.

For each metabolite ADC or D_{intra}, the *mean fit* estimates were also compared to a Gaussian distribution created from the mean and SD of the corresponding individual fits to assess the null hypothesis (mean estimate of individual fit = estimate of the *mean fit*) for a p-value of 0.05.

3 | RESULTS

To compare the spectral quality of DW-SPECIAL and STE-LASER, a diffusion set up to $b = 10\,\text{ms}/\mu\text{m}^2$ was acquired with both sequences. Good and comparable quality between the two sequences was observed at all b-values (Figure 2C). Figure S3 also shows that strong diffusion-weighting was feasible ($b = 30\,\text{ms}/\mu\text{m}^2$) with DW-SPECIAL. Although not shown here, the same quality at $b = 30\,\text{ms}/\mu\text{m}^2$ was also achieved with STE-LASER.[19] The MM contribution was higher in DW-SPECIAL due to the shorter TE (Figure 2C).

To compare the volume selection between the two sequences, the pulse profiles on the three directions were measured in one phantom experiment (Figure 2B). Similar x and z profiles and dimensions were obtained with DW-SPECIAL and STE-LASER (x: 6.4 mm for DW-SPECIAL and 6.3 mm for STE-LASER for a nominal size of 7 mm, z: 4.8 mm for DW-SPECIAL and 4.6 mm for STE-LASER for a nominal size of 5 mm). The slice-selection profile on y shows a higher contribution of signals distant from the coil (toward y positive) with STE-LASER than with DW-SPECIAL (4.1 mm and 3.8 mm, respectively) while remaining within the 5 mm nominal selection for both sequences.

To validate the J-evolution observed in the basis set simulations (Figure 3A), in vitro experiments were performed in phantoms at $b = 0.05\,\text{ms}/\mu\text{m}^2$ with both sequences (Figure 3B). The matching J-evolution patterns between the simulations and the in vitro experiments indicated that, for strongly coupled metabolites like Gln, mIns, or GABA, the shorter TE achieved in DW-SPECIAL yielded less signal loss due to J-evolution and T_2 relaxation.

To confirm experimentally the absence of cross-terms in DW-SPECIAL, the diffusion attenuation of mIns, Tau, Glu, and tCr (given as examples) was measured in vitro with both sequences (Figure S4) and compared since STE-LASER is known to have no cross-terms in the b-value. An identical diffusion decay was found for these metabolites, attesting the absence of cross-terms in DW-SPECIAL as well. This was also shown theoretically in Appendix.

To further investigate the spectral quality of single shots obtained in vivo with DW-SPECIAL, the pre-processing results with FID-A were analyzed and compared to the ones of STE-LASER. The frequency correction factors (Figure S1C) were small, stable across b-values, and similar between the two sequences (mean over all b-values: $\text{freq}_{\text{corr}} = 1.2 \pm 0.7\,\text{Hz}$ for DW-SPECIAL and $\text{freq}_{\text{corr}} = 2.1 \pm 1.7\,\text{Hz}$ for STE-LASER). The absolute phase correction factors (Figure S1D) were increasing with b-value and also comparable between

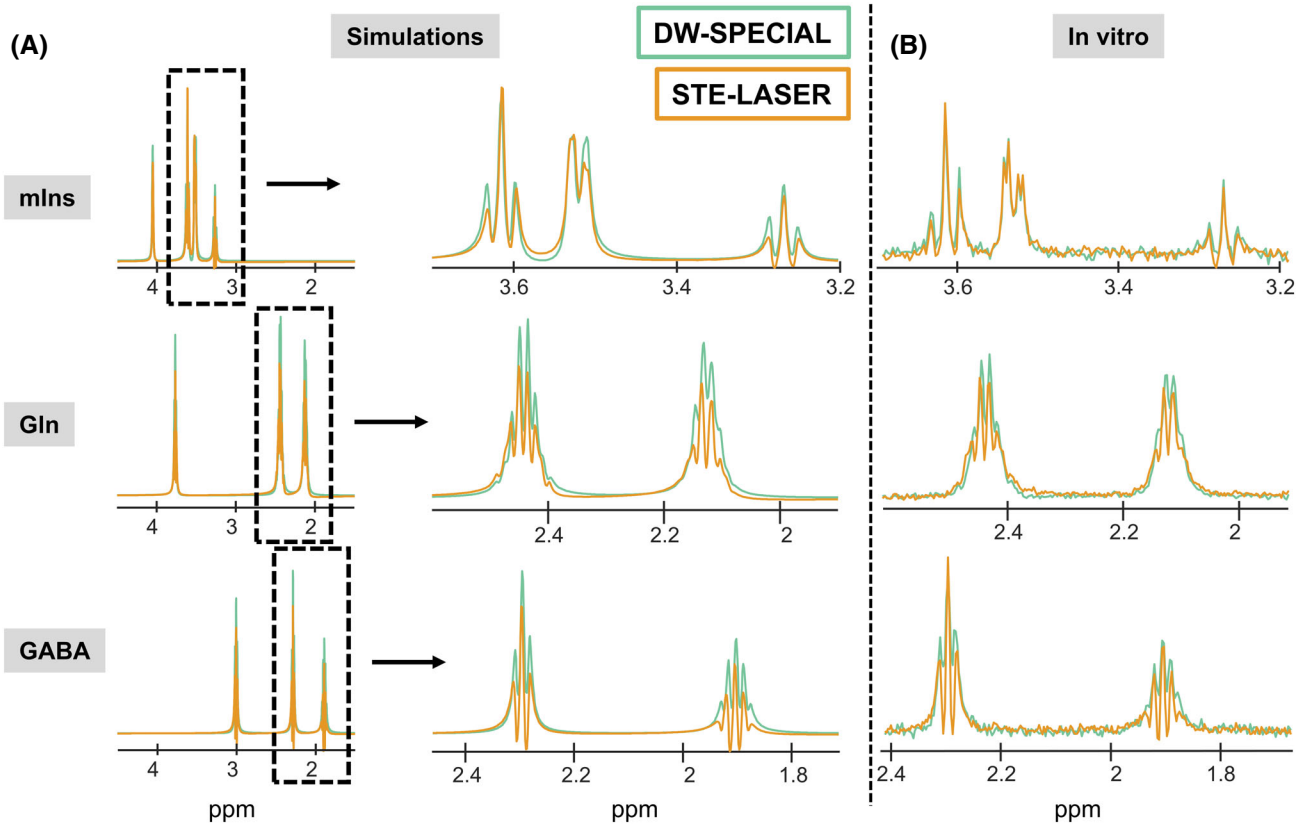

FIGURE 3 Basis set simulations (A) of some selected metabolites (mIns, Gln, and GABA) (left column), with a zoom on a multiplet region (central column) and the equivalent spectral region measured in vitro in phantoms (B) for DW-SPECIAL (green) and STE-LASER (orange). Zero-filling and a 5 Hz line broadening were applied for the simulations and a 0, 0.6, and 1.6 Hz for mIns, Gln, and GABA, respectively, for the in vitro experiments. The simulations were created with the exact delays and pulse shapes for both sequences and accounted for J-evolution but not T_2 relaxation. Simulations of Cr for both sequences featured no difference (not displayed here). The multiplet pattern measured in vitro matched the simulated ones and confirmed the reduced J-evolution in DW-SPECIAL versus STE-LASER due its shorter total TE. GABA, γ-aminobutyric acid; Gln, glutamine; mIns, myo-inositol.

sequences (at $b = 0.05\,\text{ms}/\mu\text{m}^2$: $\text{ph}_{\text{corr}} = 2.8 \pm 0.3°$ for DW-SPECIAL, and $\text{ph}_{\text{corr}} = 3.3 \pm 0.6°$ for STE-LASER, at $b = 10\,\text{ms}/\mu\text{m}^2$: $\text{ph}_{\text{corr}} = 16.1 \pm 3.0$ for DW-SPECIAL and $\text{ph}_{\text{corr}} = 24.3 \pm 8.5°$ for STE-LASER). The fraction of shots removed at each *b*-value was higher in DW-SPECIAL versus STE-LASER when performing outlier removal on individual shots (Figure S1B, top) (at $b = 0.05\,\text{ms}/\mu\text{m}^2$: $\%S_{\text{removed}} = 18.0 \pm 4.6$ for DW-SPECIAL and $\%S_{\text{removed}} = 7 \pm 0.5$ for STE-LASER, at $b = 10\,\text{ms}/\mu\text{m}^2$: $\%S_{\text{removed}} = 12.8 \pm 4.5$ for DW-SPECIAL and $\%S_{\text{removed}} = 6.3 \pm 2.8$ for STE-LASER) due to the conservative condition of removing the on/off 1D ISIS pair when at least one of the shots is corrupted. When performing outlier removal on shots already combined into pairs, the fraction of outliers removed at each *b*-value for DW-SPECIAL was similar to the one for STE-LASER (Figure S1B, bottom; Figure S1E for tabular values).

To evaluate the fit quality of the metabolite signal diffusion decays of individual animals, LCModel-relative CRLB were compared between the sequences. The fit quality improved for DW-SPECIAL compared to STE-LASER, as judged from reduced CRLB for most metabolites, with the exception of GSH, tCr, and tCho. Most noticeably, Gln CRLB were reduced irrespective of the *b*-value (Figure 4B, Gln: $\text{CRLB}_{\text{b3,STE-LASER}} = 11.2 \pm 1.9\%$, $\text{CRLB}_{\text{b3,DW-SPECIAL}} = 7.8 \pm 0.8\%$, $\text{CRLB}_{\text{b10,STE-LASER}} = 16.6 \pm 4.3$, $\text{CRLB}_{\text{b10,DW-SPECIAL}} = 11.6 \pm 1.3\%$). Metabolite signal amplitudes and CRLB tables for all reported metabolites can be found in Tables S1 and S2.

To evaluate the group variability within the diffusion data, the metabolite signal diffusion decays were further averaged across animals for each metabolite and each sequence, after normalization to $b = 0.05\,\text{ms}/\mu\text{m}^2$. Compared to STE-LASER, DW-SPECIAL reduced the group variability of diffusion decays (Figure 4A for the individual decays, Figure S5 for the mean and SD, and Table S3 for the SD tabular values) for J-coupled metabolites like Gln and mIns (Gln: $\text{SD}_{\text{b3,DW-SPECIAL}} = 0.02$ smaller than $\text{SD}_{\text{b3,STE-LASER}} = 0.13$, [$p = 0.0053$,**], $\text{SD}_{\text{b10,DW-SPECIAL}} = 0.04$ smaller than

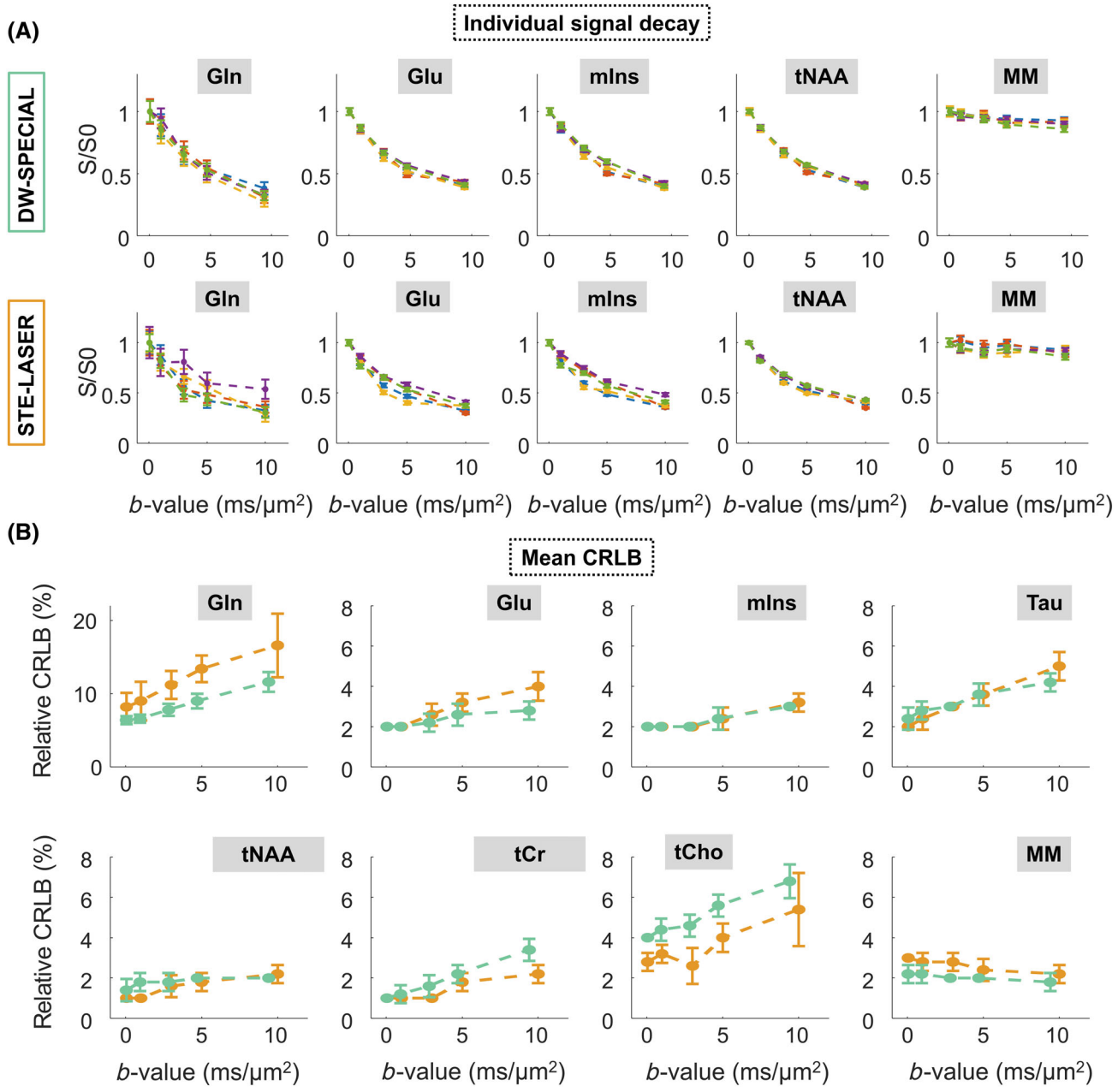

FIGURE 4 (A) Metabolite signal diffusion decays of Gln, Glu, mIns, tNAA, and MM as a function of *b*-value for all animals (different colors) and both sequences, normalized to their value at $b = 0.05\ \text{ms}/\mu\text{m}^2$. Error bars: absolute CRLB from LCModel quantification. (B) Relative CRLB (%) averaged over animals, as a function of *b*-value, for both sequences (DW-SPECIAL: green, STE-LASER: orange) and all quantified metabolites. Error bars: SD across animals at each *b*-value. For the relative CRLB, all metabolites are plotted with the same *y*-range except Gln. Of note, LCModel relative CRLB output being rounded to the nearest integer %, the SD for the CRLB is artificially high. DW-SPECIAL reduced the group variability of metabolite signal diffusion decays and improved or equaled LCModel fit quality (reduced relative CRLB) with respect to STE-LASER for all metabolites except tCho and tCr. For these two metabolites, the relative CRLB still remained low at all *b*-values for the two sequences (below 8% for tCho and below 4% for tCr). D_{intra}, intra-stick diffusivity.

$SD_{b10,\text{STE-LASER}} = 0.10$ [$p = 0.089$]) while maintaining the small variability obtained with STE-LASER for weakly coupled metabolites (tNAA) and MM.

Finally, to assess the reliability of the diffusion estimates derived from DW-SPECIAL, the ADC and D_{intra} fitted on the metabolite signal diffusion decays of individual animals and on the mean decay were compared between the sequences. DW-SPECIAL reduced the SD of estimated ADC and D_{intra} between animals (expected to be part of a homogenous control cohort) (Figure 5A,B, Gln: $SD_{ADC,\text{DW-SPECIAL}} = 0.013\ \mu\text{m}^2/\text{ms}$ smaller than $SD_{ADC,\text{STE-LASER}} = 0.073\ \mu\text{m}^2/\text{ms}$ [$p =$

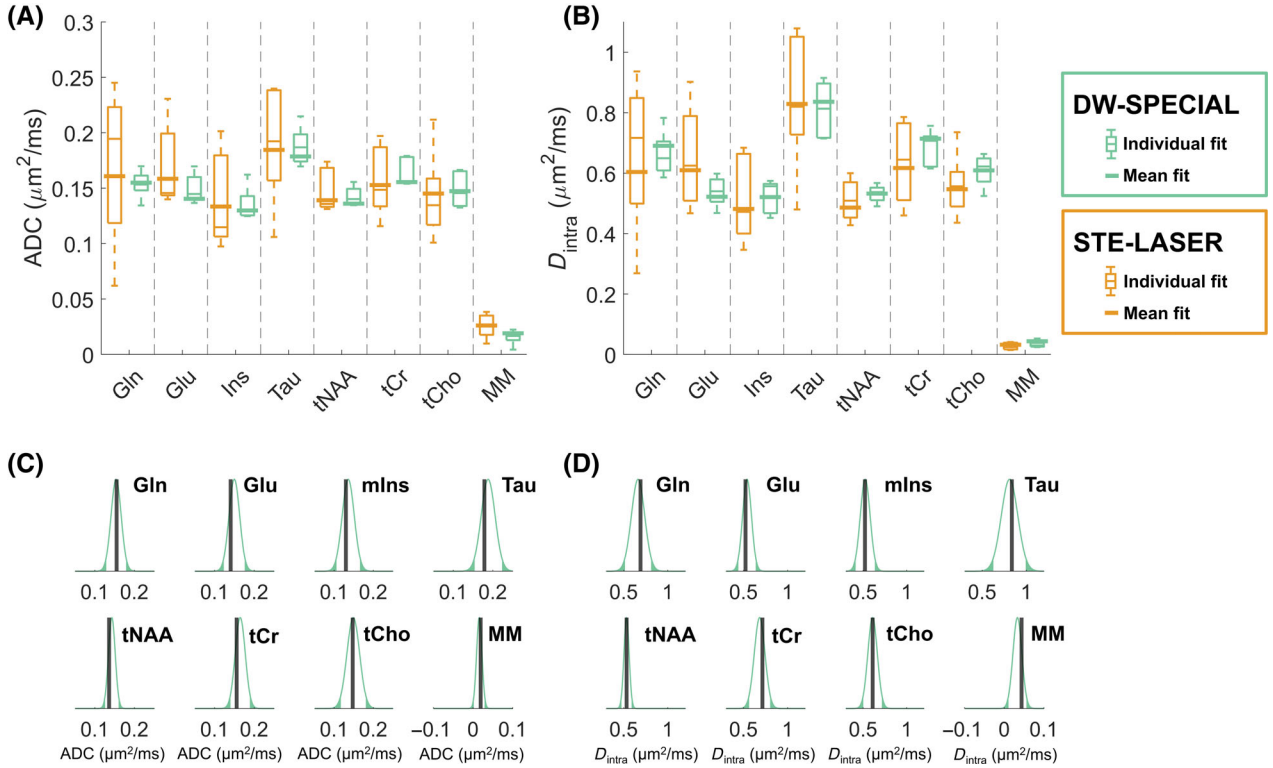

FIGURE 5 ADC (A) and D_{intra} (B) fitted for all animals with both sequences. Box plots: individual fit for each animal (line: median; top and bottom edges: 25th and 75th percentiles; whiskers: extreme values, dots: outliers (none)). Wide bar: fitted ADC and D_{intra} on the averaged diffusion decay over all animals (*mean fit*). D_{intra} from the *mean fit* was in very good agreement between the two sequences, and the SD across animals were reduced with DW-SPECIAL for all metabolites, most notably for the J-coupled ones for which the improvement is major. No statistically significant difference was found for the individually fitted ADC or D_{intra} for any of the metabolites between the two sequences ($p = 0.4$ for ADC, $p = 0.9$ for D_{intra}, two-way repeated measures ANOVA). (C, D) From the mean and SD of individual fits with DW-SPECIAL, Gaussian distributions of ADC (C) and D_{intra} (D) were generated for each metabolite and compared to the *mean fit* (wide black bar) ($p < 0.025$ regions on each side of the Gaussian distribution are dark green). The *mean fit* fell into the Gaussian distribution of the individually fitted ADC and D_{intra} ($p > 0.05$) for all metabolites, which confirmed the agreement between the estimates from the *mean fit* and from the individual fits for DW-SPECIAL. ANOVA, analysis of variance.

0.0054,**], $SD_{Dintra,DW\text{-}SPECIAL} = 0.076\,\mu m^2/ms$ smaller than $SD_{Dintra,STE\text{-}LASER} = 0.25\,\mu m^2/ms$ [$p = 0.036$,*]). No significant difference (ADC: $p = 0.4$, D_{intra}: $p = 0.9$) was found between the two sequences for the mean ADC or D_{intra} of the individual metabolite fits. For DW-SPECIAL, the *mean fit* for all metabolites was also not significantly different from the mean of ADC or D_{intra} based on individual animal fitting when assuming a Gaussian distribution around the mean and SD across animals ($p > 0.05$) (Figure 5C,D).

4 | DISCUSSION

This paper reports the first implementation and validation of a new diffusion-weighted MRS sequence, the DW-SPECIAL sequence. Our goal was to preserve the advantages of STE-LASER[19] used for rodent DWS acquisitions (absence of cross-terms, slower T_1 than T_2 relaxation during the diffusion time, good voxel localization with limited CSD artifacts, and limited sensitivity to B_1 inhomogeneities) while reaching a shorter TE. By doing so, we improved the detection and estimation of diffusion metrics of J-coupled metabolites and widened the range of investigated metabolites in rodent high-field DWS studies (e.g., to Gln, a metabolite of interest in numerous pathologies).

4.1 | Preserved advantages of the STE-LASER sequence

Our initial goal was to create a new sequence that will benefit from the advantages of STE-LASER over other conventional DWS sequences such as DW-STEAM, DW-PRESS, or DW–semi-LASER, with a shorter TE. Firstly, DW-SPECIAL allows one to reach long diffusion times, the diffusion gradients being inserted in a stimulated echo block in which the magnetization relaxes with T_1 instead of T_2 (like STE-LASER and DW-STEAM but unlike

DW-PRESS and DW-LASER). Secondly, asymmetric 90° and adiabatic 180° pulses led to a sharp volume selection and a limited CSD (like DW-LASER and DW-STEAM but unlike DW-PRESS). The slice-selection profile of the asymmetric P10 pulse[33] along the x dimension matched well the one generated by the two adiabatic 180° pulses used in STE-LASER (Figure 2B). Its large bandwidth at lower power compared to a symmetric 90° pulse limited CSD artifacts at ultrahigh field,[47] and its slice-selective nature limited the presence of spurious echoes originating from outside the volume of interest, whereas STE-LASER excites the whole volume before performing 3D localization.[22] The y profiles for both sequences are convoluted with the coil sensitivity drop at reception on the axis perpendicular to the surface coil, but the smaller contribution of signals distant from the coil with DW-SPECIAL did not substantially reduce the selected y dimension. The y profile in DW-SPECIAL was also similar to the profile shown in the SPECIAL sequence original paper.[31] The inner volume of interest signal in the y-direction accounted for approximately 75% of the total signal on y (measured with and without slice inversion), thus limiting the subtraction artifacts of the ISIS scheme (Figure S6). The z profile is expected to be similar for DW-SPECIAL and STE-LASER because this dimension is selected by a pair of adiabatic pulses in each case: the remaining difference could originate from the shift of the x and y profiles' maximum between the two sequences, leading to a contribution of signals experiencing different effective B_1 fields. To validate the voxel selection with DW-SPECIAL, the 3D profiles were measured for a smaller voxel in the same phantom ($3 \times 3 \times 3\,mm^3$) positioned in a B_1-homogeneous region. In that case, almost identical profiles were observed between DW-SPECIAL and STE-LASER for the three directions (Figure S7), further confirming the accurate volume selection with DW-SPECIAL.

Finally, an attractive aspect of the STE-LASER sequence is its block design, in which the diffusion-weighting is fully separated from the localization performed with the LASER sequence, leading to the absence of cross-terms between diffusion and imaging gradients contributing to the b-value (unlike DW-STEAM, DW-PRESS, and DW-LASER). Although this block-design was not preserved in our newly proposed sequence, the absence of cross-terms was ensured as follows: (a) the localization gradient applied during the on/off 180° ISIS pulse in the mixing time does not take part in the b-value calculation (like all other gradients in the mixing time[48]), and (b) the slice-refocusing gradient of the first slice-selective 90° P10 pulse and the first diffusion gradient (striped in Figure 1) were not applied simultaneously to prevent cross-terms originating from the first part of the STE. The absence of cross-terms was supported experimentally with the within error difference between in vitro diffusion attenuations of mIns, Tau, Glu, and tCr with DW-SPECIAL and STE-LASER and with a detailed calculation of the b-value (Figures S4 and S9) (Appendix). To minimize the increase in minimum TE caused by the separation of these two gradients, we used an asymmetric 90° pulse with an 18% refocusing factor, thus limiting the slice-selective gradient duration and contribution to the TE. The TE of the STE diffusion period was similar between the two sequences and mostly governed by the duration of the diffusion gradients. The shorter total TE achieved with DW-SPECIAL arose from the use of one pair of adiabatic pulses after the STE block, instead of three with STE-LASER.

The preprocessing yielded similar results between the two sequences (Figure S1), as measured by the amplitude of the frequency and phase-correction factors, confirming similar data quality. The frequency-drift correction was small and consistent across b-values, ascribed to the recording of a navigator scan at the end of each TR used to dynamically adjust the B_0 frequency between each acquisition. The phase fluctuations, however, increased with b-value possibly due to gradient imperfections, motion, and flow. Although the number of shots removed did not impair the spectral quality of DW-SPECIAL, a less conservative condition for outlier removal could be considered: indeed, instead of removing an ISIS on/off pair as soon as at least one of the shots is corrupted, one could either equalize, after outlier identification on each of the two subsets, the number of odd and even shots over the total number of shots, irrespective of the pairs forming each ISIS module, or perform outlier removal on already-combined pairs of shots in DW-SPECIAL (Figure S1B, bottom).

4.2 | Improved detection of J-coupled metabolites

In addition to the forementioned properties, the DW-SPECIAL sequence allows one to nearly halve the minimum TE as compared to STE-LASER (18 vs. 33 ms). As predicted by simulations, this led to an improved detection of J-coupled metabolites, such as Gln, mIns, or GABA experimentally (in phantoms [Figure 3] and in vivo [Figures 4 and 5]). To ensure a reliable comparison of the diffusion properties obtained at different TEs (here with two different sequences), there should be no correlation between the metabolites' relaxation and diffusion properties. This aspect has been investigated in vivo in the mouse brain at 11.7T[49] and showed negligible correlation between the metabolites' relaxation and diffusion properties for a range of TEs between 50 to 110 ms. We

expect that this observation can be extended to the range of TEs used in the present work (18–33 ms), at least for intracellular metabolites, thus ensuring a reliable comparison of the two sequences.

Although the LASER sequence benefits from a reduced apparent J-evolution and T_2 relaxation compared to other single-voxel spectroscopy sequences[31] at the same TE due to the succession of adiabatic 180° pulses,[50,51] and its current implementation could be further optimized,[52] the SPECIAL localization is advantageous when short TEs are desired.[22,23] At lower fields, the TE could be even further reduced by converting the pair of adiabatic pulses into a single large bandwidth asymmetric 180° (i.e., converting the semi-adiabatic SPECIAL into an asymmetric SPECIAL, as initially proposed[31]). The improvement brought by shortening the TE was particularly clear for Gln, as shown by a smaller variability of metabolite signal diffusion decays across animals (left-most panels of Figure 4A) and a better LCModel fit quality (CRLB, top left panel of Figure 4B) with DW-SPECIAL. An improved Gln quantification with shorter TE could be directly beneficial because Gln concentration is low in healthy cohorts. In hepatic encephalopathy, for example, brain Gln can be elevated by more than 100% in rodents[25] and is thus well quantified in the disease group; but it remains low in the control group, in which DW-SPECIAL could help better quantifying its diffusion properties. Importantly, although well quantified with both sequences, the within-group dispersion of Glu diffusion decays was reduced with DW-SPECIAL, possibly due to a better quantification of Gln and thus a better separation of Glx (Gln + Glu) into Gln and Glu. GABA is also strongly J-coupled and is generally not reported in diffusion studies due to its low concentration and difficult spectral resolution. Data quality obtained with DW-SPECIAL may facilitate the quantification of the diffusion decays of such low-concentrated metabolites (Figure S8) and/or the access to higher *b*-values. For the metabolites traditionally reported in rodent DWS studies (NAA, tCr, tCho, Glu, mIns, Tau), the ADC values were in good agreement with the ones measured in the mouse brain at 11.7T,[15] slightly higher in the present study due to the shorter diffusion time.

Another important feature of DW-SPECIAL is that it may render possible the fit of ADC and D_{intra} based on the metabolite signal diffusion decays of individual animals. Due to the low SNR of DWS experiments, the authors in the DWS community have traditionally fitted the diffusion coefficients on the normalized signal decay averaged over animals or subjects, or on cohort-averaged spectra. These two approaches render estimation of the uncertainty difficult. Even when error propagation or Monte Carlo simulations are used, the computed error on the diffusion coefficients may not accurately represent the dispersion within one group. The agreement between the *mean fit* and the fit on individual animals for DW-SPECIAL (Figure 5C,D) suggests that, with the spectral quality obtained herein, individual animal fitting may become feasible without a substantial penalty in accuracy.

Although the choice of the diffusion model is outside the scope of the present paper, it should be noted that the randomly oriented sticks model may not apply well to the diffusion decay of the macromolecules, which can be described by a mono-exponential decay up to high *b*-values.[53]

4.3 | Translation to human scanners and limitations

The 1D ISIS module in DW-SPECIAL makes it sensitive to motion artifacts. Although this is not a problem in general for rodent experiments in which the animal head is fixed by stereotaxic bars, additional care should be taken in human experiments.[22]

The introduction of a 90° slice-selective pulse in place of a pair of adiabatic pulses in the same direction in STE-LASER reintroduces some sensitivity to B_1 inhomogeneities. This selection should be performed on the direction with less B_1 inhomogeneities, here the *x*-direction.

OVS is generally recommended for semi-LASER (at least in the direction of the nonadiabatic slice selection)[52,54,55] and SPECIAL (at least in the ISIS and in the nonadiabatic slice selection directions).[23,31] In practice here, an OVS module in the three directions was used for both sequences. In the case of STE-LASER, this was done to prevent the creation of spurious echoes originating from outer volume signals relaxing during the mixing time and excited by the nonlocalized 90° excitation pulse in the stimulated echo diffusion block. However, OVS creates additional RF power deposition and contributes to increasing the SAR. To evaluate the contribution of the OVS module to the average RF power of each sequence, we evaluated the energy sent into the RF coils during a cycle of 160 shots for STE-LASER and DW-SPECIAL, with and without the OVS module (Table S4). A 24% lower average RF power was measured for DW-SPECIAL with OVS versus STE-LASER without OVS and a 42% lower average RF power for DW-SPECIAL with OVS versus STE-LASER with OVS (DW-SPECIAL without OVS: 7.6 mW, DW-SPECIAL with OVS: 13.1 mW, STE-LASER without OVS: 17.3 mW, STE-LASER with OVS: 22.8 mW, for a reference power of 27 mW for a 1 ms, 90° hard pulse), confirming that the train of adiabatic pulses is the main cause of elevated SAR in STE-LASER, especially at high fields.[22] In DW-SPECIAL, two pairs of 180° adiabatic pulses were replaced by an on/off adiabatic 180° pulse and

an asymmetric 90° pulse, which considerably reduced the SAR and rendered its implementation on human scanners feasible.

5 | CONCLUSION

The reduced TE achieved in DW-SPECIAL improves the detection of short T_2 and J-coupled metabolites compared to STE-LASER, the current gold standard in rodent DWS studies at high fields, while preserving the absence of cross-terms in the *b*-value. Taken together, these advantages make DW-SPECIAL a good candidate to extend the range of investigated metabolites, for example to Gln, which is rarely reported in DWS studies. We further conclude that the reduced number of RF pulses makes DW-SPECIAL an attractive alternative for human DWS studies, especially at high fields.

ACKNOWLEDGMENTS

Supported by the European Union's Horizon 2020 research and innovation program under the Marie Sklodowska-Curie, grant 813120 (INSPiRE-MED); the Swiss National Science Foundation (SNSF), projects 310030_173222, and 310030_201218; and the Leenaards and Louis-Jeantet Foundations.

We acknowledge access to the facilities and expertise of the CIBM Center for Biomedical Imaging, founded and supported by Lausanne University Hospital (CHUV), University of Lausanne (UNIL), Ecole polytechnique fédérale de Lausanne (EPFL), University of Geneva (UNIGE), and Geneva University Hospitals (HUG).

We acknowledge Stefanita Mitrea, Dario Sessa, Dr Analina Da Silva and Dr Mario Lepore for veterinary support, Dr Thanh Phong Lê for technical support, Dr Vladimir Mlynarik for experimental advice, and Dr Katarzyna Pierzchala for her help with phantom preparation. Open access funding provided by Ecole Polytechnique Federale de Lausanne.

ORCID

Jessie Mosso https://orcid.org/0000-0001-6318-9507
Dunja Simicic https://orcid.org/0000-0002-6600-2696
Bernard Lanz https://orcid.org/0000-0001-5136-075X
Cristina Cudalbu https://orcid.org/0000-0003-4582-2465

REFERENCES

1. Le Bihan D. Looking into the functional architecture of the brain with diffusion MRI. *Nat Rev Neurosci*. 2003;4:469-480.
2. Nicolay K, Braun KP, Graaf RA, Dijkhuizen RM, Kruiskamp MJ. Diffusion NMR spectroscopy. *NMR Biomed*. 2001; 14:94-111.
3. Palombo M, Shemesh N, Ronen I, Valette J. Insights into brain microstructure from in vivo DW-MRS. *Neuroimage*. 2018;182:97-116.
4. Ronen I, Valette J. Diffusion-weighted magnetic resonance spectroscopy. *eMagRes*. 2015;4:733-750.
5. Brand A, Richter-Landsberg C, Leibfritz D. Multinuclear NMR studies on the energy metabolism of glial and neuronal cells. *Dev Neurosci*. 1993;15:289-298.
6. Urenjak J, Williams SR, Gadian DG, Noble M. Proton nuclear magnetic resonance spectroscopy unambiguously identifies different neural cell types. *J Neurosci*. 1993;13:981-989.
7. Harris JL, Choi IY, Brooks WM. Probing astrocyte metabolism in vivo: proton magnetic resonance spectroscopy in the injured and aging brain. *Front Aging Neurosci*. 2015;7:202.
8. Moonen CTW, Zijl PCMV, Bihan DL, Despres D. In vivo nmr diffusion spectroscopy: 31p application to phosphorus metabolites in muscle. *Magn Reson med*. 1990;13:467-477.
9. Posse S, Cuenod CA, Le Bihan D. Human brain: proton diffusion MR spectroscopy. *Radiology*. 1993;188:719-725.
10. Ronen I, Ercan E, Webb A. Axonal and glial microstructural information obtained with diffusion-weighted magnetic resonance spectroscopy at 7T. *Front Integr Neurosci*. 2013;7:13.
11. Palombo M, Ligneul C, Hernandez-Garzon E, Valette J. Can we detect the effect of spines and leaflets on the diffusion of brain intracellular metabolites? *Neuroimage*. 2018;182:283-293.
12. Valette J, Ligneul C, Marchadour C, Najac C, Palombo M. Brain metabolite diffusion from ultra-short to ultra-long time scales: what do we learn, where should we go? *Front Neurosci*. 2018;12:2.
13. Najac C, Branzoli F, Ronen I, Valette J. Brain intracellular metabolites are freely diffusing along cell fibers in grey and white matter, as measured by diffusion-weighted MR spectroscopy in the human brain at 7 T. *Brain Struct Funct*. 2016;221:1245-1254.
14. Ronen I, Budde M, Ercan E, Annese J, Techawiboonwong A, Webb A. Microstructural organization of axons in the human corpus callosum quantified by diffusion-weighted magnetic resonance spectroscopy of N-acetylaspartate and post-mortem histology. *Brain Struct Funct*. 2014;219:1773-1785.
15. Ligneul C, Palombo M, Hernández-Garzón E, et al. Diffusion-weighted magnetic resonance spectroscopy enables cell-specific monitoring of astrocyte reactivity in vivo. *Neuroimage*. 2019;191:457-469.
16. Genovese G, Palombo M, Santin MD, et al. Inflammation-driven glial alterations in the cuprizone mouse model probed with diffusion-weighted magnetic resonance spectroscopy at 11.7 T. *NMR Biomed*. 2021;34:e4480.
17. Ligneul C, Najac C, Döring A, Beaulieu C, Branzoli F, Clarke WT, Cudalbu C, Genovese G, Jbabdi S, Jelescu I, Karampinos D, Kreis R, Lundell H, Marjańska M, Möller HE, Mosso J, Mougel E, Posse S, Ruschke S, … Valette J. Diffusion-weighted MR spectroscopy: consensus, recommendations and resources from acquisition to modelling (Version 1). 2023. https://doi.org/10.48550/ARXIV.2305.10829
18. Genovese G, Marjańska M, Auerbach EJ, et al. In vivo diffusion-weighted MRS using semi-LASER in the human brain at 3 T: methodological aspects and clinical feasibility. *NMR Biomed*. 2021;34:e4206.
19. Ligneul C, Palombo M, Valette J. Metabolite diffusion up to very high b in the mouse brain in vivo: revisiting the potential

correlation between relaxation and diffusion properties. *Magn Reson med*. 2017;77:1390-1398.
20. Slotboom J, Mehlkopf AF, Bovée WMMJ. A single-shot localization pulse sequence suited for coils with inhomogeneous RF fields using adiabatic slice-selective RF pulses. *J Magn Reson (1969)*. 1991;95:396-404.
21. Garwood M, DelaBarre L. The return of the frequency sweep: designing adiabatic pulses for contemporary NMR. *J Magn Reson*. 2001;153:155-177.
22. Öz G, Deelchand DK, Wijnen JP, et al. Advanced single voxel 1H magnetic resonance spectroscopy techniques in humans: experts' consensus recommendations. *NMR Biomed*. 2021;34:e4236.
23. Lanz B, Abaei A, Braissant O, et al. Magnetic resonance spectroscopy in the rodent brain: Experts' consensus recommendations. *NMR Biomed*. 2021; 34:e4325.
24. Norenberg MD. Distribution of glutamine synthetase in the rat central nervous system. *J Histochem Cytochem*. 1979;27:756-762.
25. Braissant O, Rackayová V, Pierzchala K, Grosse J, McLin VA, Cudalbu C. Longitudinal neurometabolic changes in the hippocampus of a rat model of chronic hepatic encephalopathy. *J Hepatol*. 2019;71:505-515.
26. Zeng G, Penninkilampi R, Chaganti J, Montagnese S, Brew BJ, Danta M. Meta-analysis of magnetic resonance spectroscopy in the diagnosis of hepatic encephalopathy. *Neurology*. 2020;94:e1147-e1156.
27. Mosso J, Yin T, Poitry-Yamate C, et al. PET CMRglc mapping and 1H-MRS show altered glucose uptake and neurometabolic profiles in BDL rats. *Anal Biochem*. 2022;647:114606.
28. Rackayova V, Braissant O, McLin VA, Berset C, Lanz B, Cudalbu C. 1H and 31P magnetic resonance spectroscopy in a rat model of chronic hepatic encephalopathy: in vivo longitudinal measurements of brain energy metabolism. *Metab Brain Dis*. 2016;31:1303-1314.
29. Mosso J, Valette J, Pierzchala K, Simicic D, Jelescu IO, Cudalbu C. Diffusion-weighted magnetic resonance spectroscopy in the cerebellum of a rat model of hepatic encephalopathy at 14.1T. In Proceedings of the 29th Annual Meeting of the ISMRM, Virtual Conference 2021. Abstract #0342.
30. Mosso J, Rey M, Simicic D, Pierzchala K, Jelescu IO, Cudalbu C. Diffusion MRI and MRS probe cerebellar microstructure alterations in the rat developing brain during hepatic encephalopathy. In Proceedings of the 30th Joint Annual ISMRM-ESMRMB Meeting, London, UK 2022. Abstract #0155.
31. Mlynárik V, Gambarota G, Frenkel H, Gruetter R. Localized short-echo-time proton MR spectroscopy with full signal-intensity acquisition. *Magn Reson med*. 2006;56:965-970.
32. Xin L, Schaller B, Mlynarik V, Lu H, Gruetter R. Proton T_1 relaxation times of metabolites in human occipital white and gray matter at 7 T. *Magn Reson Med*. 2013;69:931-936.
33. Tkác I, Starcuk Z, Choi IY, Gruetter R. In vivo 1H NMR spectroscopy of rat brain at 1 ms echo time. *Magn Reson Med*. 1999;41:649-656.
34. Kreis R, Boer V, Choi IY, et al. Terminology and concepts for the characterization of in vivo MR spectroscopy methods and MR spectra: background and experts' consensus recommendations. *NMR Biomed*. 2021;34:e4347.
35. Near J, Edden R, Evans CJ, Paquin R, Harris A, Jezzard P. Frequency and phase drift correction of magnetic resonance spectroscopy data by spectral registration in the time domain. *Magn Reson Med*. 2015;73:44-50.
36. Starčuk Z, Starčuková J. Quantum-mechanical simulations for in vivo MR spectroscopy: principles and possibilities demonstrated with the program NMRScopeB. *Anal Biochem*. 2017;529:79-97.
37. Naressi A, Couturier C, Devos JM, et al. Java-based graphical user interface for the MRUI quantitation package. *MAGMA*. 2001;12:141-152.
38. Stefan D, Cesare FD, Andrasescu A, et al. Quantitation of magnetic resonance spectroscopy signals: the jMRUI software package. *Meas Sci Technol*. 2009;20:104035.
39. Govindaraju V, Young K, Maudsley AA. Proton NMR chemical shifts and coupling constants for brain metabolites. *NMR Biomed*. 2000;13:129-153.
40. Govind V, Young K, Maudsley AA. Corrigendum: proton NMR chemical shifts and coupling constants for brain metabolites. Govindaraju V, Young K, Maudsley AA, NMR Biomed. 2000;13:129-153. *NMR Biomed*. 2015;28:923-924.
41. de Graaf RA. *In vivo NMR Spectroscopy: Principles and Techniques*. John Wiley & Sons; 2013.
42. Kunz N, Cudalbu C, Mlynarik V, Hüppi PS, Sizonenko SV, Gruetter R. Diffusion-weighted spectroscopy: a novel approach to determine macromolecule resonances in short-echo time 1H-MRS. *Magn Reson Med*. 2010;64:939-946.
43. Vanhamme L, van den Boogaart A, Van Huffel S. Improved method for accurate and efficient quantification of MRS data with use of prior knowledge. *J Magn Reson*. 1997;129:35-43.
44. Simicic D, Rackayova V, Xin L, et al. In vivo macromolecule signals in rat brain 1H-MR spectra at 9.4T: parametrization, spline baseline estimation, and T_2 relaxation times. *Magn Reson Med*. 2021;86:2384-2401.
45. Lin A, Andronesi O, Bogner W, et al. Minimum reporting standards for in vivo magnetic resonance spectroscopy (MRSinMRS): experts' consensus recommendations. *NMR Biomed*. 2021;34:e4484.
46. Callaghan PT, Jolley KW, Lelievre J. Diffusion of water in the endosperm tissue of wheat grains as studied by pulsed field gradient nuclear magnetic resonance. *Biophys J*. 1979;28:133-141.
47. Lei H, Xin L, Gruetter R, Mlynárik V. Chapter 1.2. Localized single-voxel magnetic resonance spectroscopy, water suppression, and novel approaches for ultrashort Echo-time measurements. In: Stagg C, Rothman D, eds. *Magnetic Resonance Spectroscopy: Tools for Neuroscience Research and Emerging Clinical Applications*. Academic Press; 2014:15-30.
48. Tanner JE. Use of the stimulated Echo in NMR diffusion studies. *J Chem Phys*. 1970;52:2523-2526.
49. Mougel E, Malaquin S, Valette J. Assessing potential correlation between T_2 relaxation and diffusion of lactate in the mouse brain. *Magn Reson Med*. 2022;88:2277-2284.
50. Deelchand DK, Henry PG, Marjańska M. Effect of Carr-Purcell refocusing pulse trains on transverse relaxation times of metabolites in rat brain at 9.4 Tesla. *Magn Reson Med*. 2015;73:13-20.
51. Deelchand DK, Auerbach EJ, Marjańska M. Properties of localization by adiabatic SElective refocusing (LASER) sequence. In Proceedings of the 25th Annual Meeting of ISMRM, Honolulu, HI 2017. Abstract #5585.

52. Oz G, Tkáč I. Short-echo, single-shot, full-intensity proton magnetic resonance spectroscopy for neurochemical profiling at 4 T: validation in the cerebellum and brainstem. *Magn Reson Med*. 2011;65:901-910.
53. Şimşek K, Döring A, Pampel A, Möller HE, Kreis R. Macromolecular background signal and non-gaussian metabolite diffusion determined in human brain using ultra-high diffusion weighting. *Magn Reson Med*. 2022;88:1962-1977.
54. Marjańska M, Auerbach EJ, Valabrègue R, Van de Moortele PF, Adriany G, Garwood M. Localized 1H NMR spectroscopy in different regions of human brain in vivo at 7 T: T_2 relaxation times and concentrations of cerebral metabolites. *NMR Biomed*. 2012;25:332-339.
55. Scheenen TWJ, Klomp DWJ, Wijnen JP, Heerschap A. Short echo time 1H-MRSI of the human brain at 3T with minimal chemical shift displacement errors using adiabatic refocusing pulses. *Magn Reson Med*. 2008;59:1-6.

SUPPORTING INFORMATION

Additional supporting information may be found in the online version of the article at the publisher's website.

Figure S1. Processing results for the two sequences. (A): Visualization of the processing results for one spectrum at $b = 0.05\ \text{ms}/\mu\text{m}^2$ acquired with DW-SPECIAL. The on and off shots were processed separately but combined here for the display. (B): Fraction (in %) of motion-corrupted shots removed for each sequence, one dot per animal and *b*-value, one color per *b*-value, performed either before shot combination into each pair (top, "individual shots") or after shot combination into each pair (bottom, "combined shots") in DW-SPECIAL. (C): Frequency correction factors (absolute value) found by spectral registration in FID-A, mean and SD across shots, one error-bar per animal and *b*-value, one color per *b*-value. (D): Phase correction factors (absolute value) found by spectral registration in FID-A, mean and SD across shots, one error-bar per animal and *b*-value, one color per *b*-value. The frequency and phase factors are displayed in absolute value but all the distributions are centred on 0. (E): Tabular mean values for panel (B). Due to the conservative condition of removing the on/off 1D ISIS pair when at least one of the shots is corrupted, the number of shots removed at each *b*-value is higher in DW-SPECIAL versus STE-LASER. Yet, when performing outlier removal on combined shots, the two sequences performed similarly (panel B, bottom). Similar phase and frequency correction factors are obtained with both sequences, with more outlier values for STE-LASER, confirming the good data quality of DW-SPECIAL.

Figure S2. Validation of metabolite residuals removal on the macromolecule spectrum using multiple double inversion recovery experiments (A) and with high/low diffusion-weighting (B). In (A), the first TI delay was fixed to 2200 ms and the second TI delay was varied (colors) to identify the metabolites residuals, also following Cudalbu et al. and Simicic et al. (https://doi.org/10.1002/nbm.4393 and https://doi.org/10.1002/mrm.28910). In (B), the second TI delay was fixed to 850 ms (the one featuring the least metabolite residuals, the one chosen in the present manuscript) and the macromolecular spectrum was acquired with high/low diffusion-weighting to confirm the pattern of metabolites removal found in (A). For visual inspection, the amplitude of the MM at 0.9 ppm was matched for the two conditions.

Figure S3. Representative DW-SPECIAL diffusion spectra after processing (ECC, phase and frequency alignment and motion-corrupted shots removal), for four *b*-values, plotted with 5 Hz line broadening. Metabolites with relative CRLB below 10% at $b = 0.05\ \text{ms}/\mu\text{m}^2$ are labeled on the first panel. The spectrum at $b = 30\ \text{ms}/\mu\text{m}^2$ acquired in one animal is shown here as a proof of feasibility. The diffusion spectra are of good quality and the increasing contribution of the macromolecules with respect to the metabolites can be observed with increasing *b*-values as a result of their slower diffusivity.

Figure S4. Phantom experiment confirming the absence of cross-terms in DW-SPECIAL. A phantom mimicking realistic in vivo metabolite concentrations (left panel, 4 Hz line broadening for visualization) was scanned with DW-SPECIAL and STE-LASER, the latter featuring no cross-terms in the *b*-value as previously shown in Ligneul et al. (https://doi.org/10.1002/mrm.26217). The example diffusion attenuations over *b*-value (after normalization to the first *b*-value) for mIns, Tau, Glu, and tCr after LCModel quantification show no difference between the two sequences, confirming the absence of cross terms in DW-SPECIAL as well. The small offset observed for mIns could have been caused by a quantification error in the first point for either one of the sequences.

Figure S5. Normalized metabolite signal diffusion decays averaged over animals, as a function of *b*-value, for both sequences (DW-SPECIAL: green, STE-LASER: orange) and all quantified metabolites. Error bar: SD of S/S_0 values across animals at each *b*-value. It contains the same information as Figure 4A, displayed here as mean and SD across animals.

Figure S6. Estimation of outer versus inner VOI signal contributions on the *y*-direction in DW-SPECIAL. Non-localized estimation based on the water signal in a phantom (absolute value of the spectrum) measured on an odd (blue, S_0) and on an even shot (green, S_1). The single-shot intra VOI signal is given by $0.5 \times (S_0 + S_1)$ and the single-shot extra VOI signal is given by $0.5 \times (S_0 - S_1)$. Note that the receiver phase shift is included in the even shots such that the intra VOI signal is given by the sum of 2 consecutive shots (instead of the difference). f_{intra} is 77%: the main contribution of the signal on *y* comes from

inside the VOI, which limits the subtraction artifacts in the ISIS scheme. In vivo, the signal will in addition be weighted by the spatial variations of water and metabolite concentrations.

Figure S7. 1D projections of the *x, y, z* selection profiles for a small voxel ($3 \times 3 \times 3\ mm^3$) in a B_1-homogeneous region measured with DW-SPECIAL (green) and STE-LASER (orange) in the multi-metabolite phantom. The profiles are obtained by switching on the corresponding gradient during the acquisition. The integral values of the profile shapes are displayed. The dashed black lines represent the nominal voxel position in each direction. Negligible difference is observed in the voxel selection between the two sequences when the factor of B_1 inhomogeneity is removed, confirming the good selection performed with DW-SPECIAL.

Figure S8. Signal diffusion decays of Asc, Lac, GSH, and GABA as a function of *b*-value for all animals (different colors) and both sequences, normalized to their value at $b = 0.05\ ms/\mu m^2$. Error bars: absolute CRLB from LCModel quantification. Although these metabolites are generally not reported in DWS studies owing to their low concentration and poor quantification, the shorter TE achieved in DW-SPECIAL leads to a smaller within-group dispersion of their diffusion decays and suggests that these metabolites could possibly be investigated in future studies (through a fit of the mean diffusion decay).

Figure S9. (Appendix). Possible positions for the slice-refocusing gradient of the first slice-selective 90°. (A): slice-refocusing gradient applied before the diffusion gradient, which is the option chosen for DW-SPECIAL and yields to no-cross term. (B): slice-refocusing gradient and the first diffusion gradient applied simultaneously, allowing to reduce the minimum TE but yielding to cross-terms.

Table S1. Signal amplitudes and relative Cramer Rao Lower Bounds from LCModel fit of DW-SPECIAL spectra averaged over animals at all *b*-values and for every reported metabolite. Metabolite signals are not referenced to water and their amplitudes are in arbitrary unit: only their relative amplitudes at $b = 0.05\ ms/\mu m^2$ is of biological relevance. The MM basis-set spectrum was scaled such that its concentration at $b = 0.05\ ms/\mu m^2$ is in the range 1–4 mM (Cudalbu et al., https://doi.org/10.1002/nbm.4393).

Table S2. Signal amplitudes and relative Cramer Rao Lower Bounds from LCModel fit of STE-LASER spectra averaged over animals at all *b*-values and for every reported metabolite. Metabolite signals are not referenced to water and their amplitudes are in arbitrary unit: only their relative amplitudes at $b = 0.05\ ms/\mu m^2$ is of biological relevance. The MM basis-set spectrum was scaled such that its concentration at $b = 0.05\ ms/\mu m^2$ is in the range 1-4 mM (Cudalbu et al., https://doi.org/10.1002/nbm.4393).

Table S3. SD of normalized signal diffusion decays over animals at all *b*-values and for every reported metabolite, for DW-SPECIAL and STE-LASER.

Table S4. Average power in mW measured in a phantom as the total energy deposited in the RF coils during 160 TR, for the typical RF loading of an in vivo experiment (reference power for a 90° square pulse [1 ms]: 27 mW). This measurement was done with the RF duty cycle tool in PV360 v3.3 for both sequences with and without OVS. The RF power deposition is lower for DW-SPECIAL with OVS than for STE-LASER without OVS, thus demonstrating the benefits of DW-SPECIAL over STE-LASER for SAR considerations.

Table S5. MRSinMRS checklist from Lin et al. « Minimum Reporting Standards for in Vivo Magnetic Resonance Spectroscopy (MRSinMRS): Experts' Consensus Recommendations ».

How to cite this article: Mosso J, Simicic D, Lanz B, Gruetter R, Cudalbu C. Diffusion-weighted SPECIAL improves the detection of J-coupled metabolites at ultrahigh magnetic field. *Magn Reson Med*. 2023;1-15. doi: 10.1002/mrm.29805